1 **Revision 1**

2 **Temperature and compositional dependences of H$_2$O solubility in majorite (Word**

3 **Count: 5387)**

4 **Dan Liu[1-3], Narangoo Purevjav[3], Hongzhan Fei[3,4], Anthony C. Withers[3], Yu Ye[2], Tomoo**

5 **Katsura[3]**

6 [1]Gemmological Institute, China University of Geosciences, Wuhan, 430074, China

7 [2]State Key Laboratory of Geological Processes and Mineral Resources, China University of

8 Geosciences, Wuhan, 430074, China

9 [3]Bayerisches Geoinstitut, University of Bayreuth, Bayreuth, 95440, Germany

10 [4]Key Laboratory of Geoscience Big Data and Deep Resource of Zhejiang Province, School of

11 Earth Sciences, Zhejiang University, Hangzhou, 310058, China

12

13 Corresponding author:

14 Dan Liu (danliu@cug.edu.cn)

15 Narangoo Purevjav (Narangoo.Purevjav@uni-bayreuth.de)

16

17   **Abstract**

18   We systematically investigated H_2O solubility in majorite as a function of temperature at 1670 –

19   2270 K under a pressure condition of 20 GPa using multi-anvil experimental techniques. The

20   H_2O solubility in majorite decreases with increasing temperature. In addition, the H_2O content is

21   relatively independent of the concentrations of Al_2O_3 and SiO_2 in majorite. Majorite can store

22   more H_2O than bridgmanite in the lower mantle. Therefore, when a slab sinks into the lower

23   mantle, hydrous melt could be produced not only by the phase transformation from ringwoodite

24   to bridgmanite + ferropericlase near 660-km depth, but also by the majorite to bridgmanite

25   transformation over a wide range of depth from 660 km up to ~800 km, at which depth majorite

26   dissolves completely in bridgmanite.

27
28   **Keywords**: majorite; H_2O solubility; transition zone; hydrous melt
29

30   **1 Introduction**

31   The mantle transition zone is a potential H_2O reservoir in the Earth's interior (e.g., Fei et

32   al. 2017; Hirschmann 2006; Pearson et al. 2014) because the H_2O solubility of its dominant

33   minerals, wadsleyite and ringwoodite, reaches 1 ~ 2 wt.% (Demouchy et al. 2005; Druzhbin et

34   al. 2021; Fei and Katsura 2020a, 2021; Kohlstedt et al. 1996; Litasov et al. 2011; Purevjav et al.

35   2014, 2016). The H_2O solubility refers to the H_2O content of a mineral equilibrated with hydrous

36   melt (Hirschmann et al. 2005). These values are distinctly higher than those of other major

37   mantle minerals such as olivine, pyroxene, bridgmanite, and ferropericlase (Fei and Katsura

38   2020b; Férot and Bolfan-Casanova 2012; Fu et al. 2019; Guo et al. 2020; Kohlstedt et al. 1996;

39   Litasov 2010; Liu et al. 2021; Purevjav et al. 2023; Smyth et al. 2006; Withers and Hirschmann

40   2008). Therefore, hydrous melts are expected to be formed by a back transformation at 410 km

41   depth from wadsleyite to olivine and a forward transformation at 660 km depth from ringwoodite

42   to bridgmanite + ferropericlase. The presence of hydrous melt may affect mantle dynamics

43   significantly (Revenaugh and Sipkin 1994; Schmandt et al. 2014; Vinnik and Farra 2007).

44   Majorite, which contributes up to ~40 vol.% of the transition zone, persists in the lower

45   mantle down to ~800 km depth until the dissolution of majorite in bridgmanite is completed

46   (Ishii et al. 2018, 2019; Ringwood 1991; Stixrude and Lithgow-Bertelloni 2007). As majorite

47   may contain higher amounts of H_2O than bridgmanite (Fu et al. 2019; Katayama et al. 2003; Liu

48   et al. 2021), a hydrous melt may be produced by the majorite-bridgmanite transformation

49   (Panero et al. 2020).

50   Nevertheless, the H_2O solubility of majorite is poorly constrained, while the H_2O

51   solubility of wadsleyite and ringwoodite has been studied extensively. Katayama et al. (2003)

52   reported an H_2O solubility of about 1200 wt. ppm in majorite, but their temperature range was

53   limited (1670 - 1770 K). Accordingly, the temperature dependence is unknown despite the fact

54   that the H_2O solubility in minerals is strongly correlated to temperature (e.g., Demouchy et al.

55   2005; Fei and Katsura 2020a, 2021; Litasov et al. 2011). Moreover, even though the composition

56   of majorite can vary significantly in the Earth's mantle (Frost 2008), the compositional

57   dependence of H_2O solubility is also unknown. Therefore, a systematic study of the effects of

58   temperature and composition on H_2O solubility in majorite is required to assess hydrous melting

59   at the top of the lower mantle.

60   In this study, we determined the temperature and compositional dependences of H_2O

61   solubility in majorite at temperatures of 1670 to 2270 K and a pressure of 20 GPa using a multi-

62   anvil press. Our results suggest that majorite can store 900 ~ 3000 wt. ppm H_2O in the deep

63   mantle and may play an important role in the dehydration melting at the topmost lower mantle.

64   **2 Materials and Methods**

65   **2.1 Starting material**

66   Four compositionally different starting materials, hereafter referred to as starting

67   materials A, B, C, and D, were prepared from SiO_2, FeO, Al_2O_3, $Mg(OH)_2$, and $Ca(OH)_2$

68   powders (Table 1). The SiO_2 and Al_2O_3 powders were heated at 1270 K for two hours in an

69   ambient-pressure furnace, whereas the $Mg(OH)_2$ and $Ca(OH)_2$ powders were heated at 400 K in

70   a vacuum oven prior to use. The five powders were weighed and then well-mixed by grinding in

71   an agate mortar. Starting material A had a bulk composition close to pyrolite-minus-olivine

72   (Irifune and Ringwood 1987) plus H_2O. Starting material B had a lower Al_2O_3 content because

73   the Al_2O_3 component tends to be incorporated in majorite rather than melt. Starting materials C

74   and D had higher MgO and CaO contents and lower SiO_2 contents to suppress the formation of

75   stishovite in the run products. The bulk H_2O contents were all 12 wt.%. All the mixed powders

76   were stored in a vacuum oven at 400 K before use.

77

78   **2.2 High-pressure experiments**

79   High-pressure experiments were carried out in a 1000-ton multi-anvil press at the

80   Bayerisches Geoinstitut, University of Bayreuth. The starting materials were welded into $Pt_{95}Rh_5$

81   capsules with inner and outer diameters of 1.0 and 1.2 mm, respectively. The capsule lengths

82   after completion were 1.0 - 1.2 mm, except for run H5405, in which the capsule length was 2.0

83   mm. The sample assembly consisted of a Cr_2O_3-doped MgO octahedral pressure medium with an

84   edge length of 10 mm, a ZrO_2 sleeve for thermal insulation, and a $LaCrO_3$ heater. One or two

85   capsules were loaded into an MgO sleeve in the heater. The assembly was pressurized to a

86   pressure of 20 GPa using eight tungsten carbide anvils with truncated edge lengths of 4 mm,

87   followed by heating to target temperatures of 1670 to 2270 K with a ramp rate of 70 K/min.

88   Temperatures were monitored using a type-D (W97Re3/W75Re25) thermocouple. The run

89   duration at the target temperature was 20 or 24 hours.

90

91   **2.3 Sample analyses**

92   The recovered run products were embedded in epoxy resin, and cross-sections were

93   prepared by grinding using silicon carbide grinding paper and lapping using diamond powder.

94   The phases present in the capsules were identified using a Bruker AXS D8 Discover micro-

95   focused X-ray diffractometer (XRD) equipped with a two-dimensional solid-state detector and a

96   Co-Kα radiation source operated at 40 kV and 500 μA. An example of the XRD patterns is

97   shown in **Fig. 1a**.

98   The textures of the samples within the capsules were observed using a scanning electron

99   microscope (SEM) with a backscattered-electron detector (BSE). The BSE images of all

100   recovered capsules can be found in the Supplementary Materials (**Fig. S1**), with an example

101   given in **Fig. 1b.** The phases identified by XRD were also confirmed by compositional

102   measurements using an energy-dispersive X-ray spectrometer (EDS).

103   Chemical compositions of the run products were obtained using a JEOL JXA-8200

104   electron probe microanalyzer (EPMA) equipped with wavelength-dispersive spectrometers

105   (WDS) operated at an acceleration voltage of 15 kV and a beam current of 15 nA. Enstatite was

106   used as a standard for Mg and Si, and corundum, metallic Fe, and diopside for Al, Fe, and Ca,

107   respectively. A focused beam was used to analyze the solid phases, while a defocused beam was

108   used for the melt phase. The counting time for each analysis was 20 sec.

109

110   **2.4 Determination of H₂O contents in majorite**

111   The H₂O contents in majorite were determined by Fourier-transform infrared (FTIR)

112   spectroscopy analysis using a Bruker IFS 120 high-resolution spectrometer coupled with a

113   Bruker IR microscope. After polishing to thicknesses of 50-100 μm, unpolarized FTIR spectra

114   were taken on the samples. Any inclusions or microcracks visible under an optical microscope

115   were avoided in the analysis. Infrared analyses were made using a visible light source, CaF_2

116   beamsplitter, and liquid-N_2-cooled MCT detector. Each spectrum was collected by accumulating

117   100 scans at a resolution of 2 cm⁻¹. Two to six spectra were collected for each sample.

118   Peak-fitting of the FTIR spectra was performed by fitting the sum of two Gaussian

119   functions. The first peak at a wavenumber of 3615 cm⁻¹ is related to hydrogen in majorite

120   (Bolfan-Casanova et al. 2000; Liu et al. 2021), while the second at a wavenumber of 3430 cm⁻¹ is

121   expected to be from inclusions or sub grain boundaries which are invisible under the optical

122   microscope (Katayama et al. 2003; Liu et al. 2021).

123   Subsequently, the H₂O content C_{H_2O} in majorite, expressed as wt. ppm H₂O, was

124   calculated using the Beer-Lambert law,

125    $$C_{H_2O} = \frac{10^6 \times 18.02}{\varepsilon \tau \rho} \times \int H(v)\mathrm{d}v, \qquad (1)$$

126   where $H(v)$ is the infrared absorbance of the sample at a wavenumber of v, ε is the integral molar

127   absorption coefficient (see below), τ is the sample thickness, and ρ is the density (3670 g/L). The

128 integration was made for the infrared absorption bands at 3615 cm^{-1} given by the peak-fitting

129 process.

130   Thomas et al. (2015) reported a wavenumber-dependent infrared absorption coefficient

131 for majorite, which was ε = 6000 L/(mol.cm^2) at a v = 3615 cm^{-1}. This value was used for the

132   calculation of C_{H_2O} in this study. The C_{H_2O} was also calculated using the calibrations reported by

133 Bell et al. (1995) (specific to garnet) and by Paterson (1982) (for general silicate minerals and

134 glasses) and listed in Table 2 for comparison.

135

136 **3 Results and discussion**

137   **3.1 Phase assemblages of the run products**

138   Majorite crystals with grain sizes of 50 ~ 300 μm coexisting with hydrous melts

139 (crystallized to small grains during quenching) were found in all of the recovered capsules

140 (**Table 2, Fig. 1, Fig. S1**), indicating that experiments were H$_2$O-saturated. Stishovite crystals

141 appeared in the experiments with high SiO$_2$-content starting materials A and B, while

142 davemaoite (CaSiO$_3$ perovskite) appeared in the experiments with low SiO$_2$-content starting

143 materials C and D. Magnesite and dense hydrous magnesium silicate phases (superhydrous phase

144 B and phase D) were formed under relatively low-temperature conditions (1670 K) with starting

145 material of C (**Table 2**).

146

147   **3.2 Chemical compositions of majorite**

148   Since compositionally different starting materials were used, the composition of majorite

149 and melt from different runs cannot be compared directly (**Table 3, Table 4**). However, the

150 composition of majorite synthesized from the same starting material (B) shows a systematic

151 change with temperature, i.e., the Si atomic concentration increases, while the Al and Fe

152 concentrations decrease with increasing temperature. Meanwhile, the Mg concentration increases

153 from 1670 to 1870 K and decreases at higher temperatures, whereas the Ca concentration shows

154 an opposite trend to Mg (**Fig. 2**).

155   The atomic concentrations of Si and Mg+Fe+Ca, where Fe is assumed to be ferrous, are

156 plotted against the Al concentration for all samples (**Fig. 2**). It is found that both Mg+Fe+Ca and

157 Si concentrations are inversely correlated with the Al concentrations, indicating the dilution of

158 Al_2O_3 by the incorporation of the $(Mg,Fe,Ca)SiO_3$ component in majorite.

159

160   **3.3 FTIR spectra of majorite**

161   All of the majorite samples obtained in this study show asymmetric infrared absorption

162 bands between 3000 and 3800 cm^{-1} with peak positions at 3610~3120 cm^{-1} and a broad shoulder

163 from about 3500 to 3000 cm^{-1} (**Fig. 3**). Although the shapes and peak positions in the spectra are

164 identical in different samples, suggesting the same dominant proton incorporation mechanisms in

165 majorite with different compositions, the peak height decreases with increasing temperature,

166 indicating temperature-dominated water contents of the samples in this study.

167   By deconvolution of the spectra, the infrared absorption peak at 3615 was obtained,

168 which could be attributed to majorite (Bolfan-Casanova et al. 2000; Liu et al. 2021). In contrast,

169   Thomas et al. (2015) and Katayama et al. (2003) reported infrared absorption peaks at slightly

170   lower wavenumbers (3550 ~ 3580 cm^{-1}). The 3430 cm^{-1} peak likely arises from H_2O in

171   inclusions, so it was not considered for the calculation of water content in this study. Even

172   though we have followed previous studies in assigning the broad absorption band to water H_2O

173   from inclusions (Liu et al. 2021), we cannot rule out a contribution from bonded hydroxyl in

174   majorite. If the broad absorption band is included in the calculation of C_{H_2O}, the values are

175   roughly doubled.

176   **3.4 Temperature dependence of H_2O solubility in majorite**

177   Although the water solubility in majorite has already been reported previously (Bolfan-

178   Casanova et al. 2000; Katayama et al. 2003; Panero et al. 2020; Thomas et al. 2015), all previous

179   studies focused on a fixed temperature or composition without a systematic investigation. Since

180   majorite coexists with hydrous melt in all runs in this study, the H_2O contents obtained in this

181   study should represent the H_2O solubility of majorite under the corresponding pressure and

182   temperature conditions. Based on the FTIR calibration of Thomas et al. (2015), the H_2O content

183   in our majorite samples decreases from about 2900 to 400 wt. ppm with increasing temperature

184   from 1670 to 2270 K, regardless of the difference in starting materials (**Table 1**, **Fig. 4**).

185   Therefore, our results indicate a systematic decrease of H_2O solubility in majorite with

186   temperature.

187   The temperature dependence of H_2O solubility can be understood thermodynamically.

188   Majorite is equilibrated with melt by the reaction,

189   Silicate (Majorite) + H_2O (melt) = H_2O (majorite) + silicate (melt) (2)

9
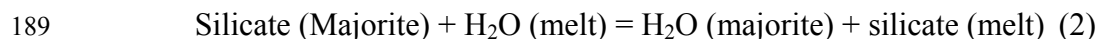
190   Assuming that activity is proportional to mole fraction, the change in Gibbs energy of the

191   above reaction ($\Delta G_{(2)}$) is,

192    $$\Delta G_{(2)} = -RT\ln\frac{C_{H2O}^{maj} \times C_{Silicate}^{melt}}{C_{H_2O}^{melt} \times C_{silicate}^{maj}} \qquad (3)$$

193   where C_M^N is the fraction of the component of M in the phase N. Because of $C_{silicate}^{maj} \approx 1$,

194   we have,

195    $$C_{H2O}^{maj} = \frac{C_{H_2O}^{melt}}{C_{silicate}^{melt}} \exp(-\frac{\Delta G_{(2)}}{RT}) \qquad (4)$$

196    $C_{H_2O}^{melt}$ should decrease with increasing temperature as the melt fraction increases (e.g.,

197   Fei 2021; Hirschmann et al. 2005), resulting in the decrease of $\frac{C_{H_2O}^{melt}}{C_{silicate}^{melt}}$ with temperature. On the

198   other hand, H$_2$O is preferentially incorporated in melt rather than solid minerals, thus, $\Delta G_{(2)} > 0$.

199   As a result, $C_{silicate}^{melt}$ decreases with temperature approximately following a logarithmic function.

200   The fitting of data points gives,

201    $$C_{H_2O}^{maj} = exp\left(\frac{9810}{T} + 1.90\right) \qquad (5)$$

202   where $C_{H_2O}^{maj}$ is the H$_2$O content in majorite based on the FTIR calibration of Thomas et

203   al. (2015).

204   We emphasize that the C_{H2O} determined from infrared spectroscopy relies on the FTIR

205   calibrations, i.e., the infrared absorption coefficients reported previously. Using different

206   absorption coefficients (e.g., Bell et al. 1995; Paterson 1982) linearly affects the absolute values

207   of H$_2$O solubility (**Table 2**). However, the temperature dependence should remain the same. We

208   also note that the H$_2$O solubility in majorite determined in this study is within the experimental

10

209   uncertainty comparable with those of Katayama et al. (2003), Thomas et al. (2015), Panero et al.

210   (2020), and Liu et al. (2021) at identical temperatures, In the referenced studies, H_2O contents

211   were determined by secondary ion mass spectrometry, electron recoil detection analysis, and

212   infrared spectroscopy. Therefore, the different techniques for C_{H2O} determination should not

213   affect our conclusion significantly.

214

3.5 Compositional dependence of C_{H2O} and the proton incorporation mechanism

216   Although different starting materials were used in this study, resulting in compositionally

217   different majorite samples, the C_{H2O} in the run products do not show systematic variations with

218   composition (**Fig. 5**). This suggests that protons in majorite are incorporated into the

219   dodecahedral and/or tetrahedral sites ($M^{2+}_{VIII} \leftrightarrow (2H^+)_{VIII}$ and $Si^{4+}_{IV} \leftrightarrow (4H^+)_{IV}$, respectively)

220   rather than the coupled $H^+ + Al^{3+}$. This is because if Si^{4+} or divalent cations (M^{2+}) were

221   substituted by $H^+ + Al^{3+}$, the H_2O content would be positively correlated with the Al_2O_3 content,

222   which is not the case in this study (**Table 3**).

223   The $Si^{4+}_{IV} \leftrightarrow (4H^+)_{IV}$ substitution (hydrogarnet substitution) is more likely in this study

224   because it shows an infrared absorption band at 3630 cm^{-1} in pyrope (Ackerman et al. 1983;

225   Geiger and Rossman 2018), similar to the infrared absorption peaks for majorite (**Fig. 3**). The

226    $Si^{4+}_{IV} \leftrightarrow (4H^+)_{IV}$ substitution is also suggested by first-principle calculations, which show that

227   the $(4H^+)_{IV}$ defect is more energetically favorable than the $(2H^+)_{VIII}$ defect in $MgSiO_3$-majorite

228   (Pigott et al., 2015).

229

4 Implications for the role of majorite for water storage in the deep mantle

230

231   Majorite is an important mineral in the mantle transition zone and the topmost lower

232 mantle (Irifune and Ringwood 1987; Ringwood 1991), corresponding to a temperature condition

233 of 1800 ~ 2000 K according to the typical mantle geotherm (Katsura 2022). Over this

234 temperature range, majorite can contain about 900 ~ 1500 wt. ppm. This value is much lower

235 than wadsleyite and ringwoodite, the dominant minerals in the mantle transition zone (~1.0

236 wt.%, Demouchy et al. 2005; Druzhbin et al. 2021; Fei and Katsura 2020, 2021; Kohlstedt et al.

237 1996; Litasov et al. 2011). However, H_2O solubility is significantly higher than in bridgmanite

238 (<100 ~ 900 wt. ppm, Fu et al. 2019; Liu et al. 2021; Purevjav et al. 2023) and ferropericlase

239 (<100 wt. ppm, Bolfan-Casanova et al. 2002, 2003; Litasov et al. 2010) in the lower mantle.

240 Therefore, majorite is expected to be the major H_2O reservoir in the topmost lower mantle within

241 its stability field, i.e., down to ~800 km depth before complete phase transformation to

242 bridgmanite (Ishii et al. 2018, 2019; Ringwood 1991; Stixrude and Lithgow-Bertelloni 2007).

243   H_2O can be transported into the deep mantle by slab subduction. When slabs sink into the

244 lower mantle, hydrous ringwoodite within the slabs transforms to bridgmanite and ferropericlase,

245 forming a hydrous melt layer just below the 660-km discontinuity due to the contrasting H_2O

246 solubilities in ringwoodite, bridgmanite, and ferropericlase (Schmandt et al. 2014). The hydrous

247 melt should saturate majorite within the slabs. Due to the relatively low temperature of slabs

248 (~1600 K near the 660 km discontinuity, Litasov et al. 2013; Tan et al. 2002), majorite can

249 contain about 3000 wt. ppm H_2O, which is significantly higher than bridgmanite (Fu et al. 2019;

250 Liu et al. 2021; Purevjav et al. 2023). As majorite transforms to bridgmanite gradually, a thick

251 hydrous melt layer is expected at the top of the lower mantle depths of 660 ~ 800 km (Panero et

252 al. 2020), which may lower the slab viscosity significantly.

253

Acknowledgments

263

Reference

265   Ackermann, L., Cemič, L., and Langer, K. (1983). Hydrogarnet substitution in pyrope: a possible

266   location for "water" in the mantle. Earth and Planetary Science Letters, 62(2), 208–214.

267   Bell, D.R., Ihinger, P.D., and Rossman, G.R. (1995). Quantitative analysis of trace OH in garnet

268   and pyroxenes. American Mineralogist, 80(5-6), 465–474.

269   Bolfan-Casanova, N., Keppler, H., and Rubie, D.C. (2000). Water partitioning between

270   nominally anhydrous minerals in the $MgO-SiO_2-H_2O$ system up to 24 GPa: implications for

271   the distribution of water in the Earth's mantle. Earth and Planetary Science Letters, 182(3),

272   209–221.

273   Bolfan-Casanova, N., Keppler, H., and Rubie, D.C. (2003). Water partitioning at 660 km depth

274   and evidence for very low water solubility in magnesium silicate perovskite. Geophysical

275   Research Letter, 30, 1905.

276   Bolfan-Casanova, N., Mackwell, S., Keppler, H., McCammon, C., and Rubie, D.C. (2002).

277   Pressure dependence of H solubility in magnesiowüstite up to 25 GPa: implications for the

278   storage of water in the Earth's lower mantle. Geophysical Research Letter, 29 (10), 1449.

279   Demouchy, S., Deloule, E., Frost, D.J., and Keppler, H. (2005). Pressure and temperature-

280   dependence of water solubility in Fe-free wadsleyite. American Mineralogist, 90(7), 1084–

281   1091.

282   Druzhbin, D., Fei, H., and Katsura, T. (2021). Independent hydrogen incorporation in wadsleyite

283   from oxygen fugacity and non-dissociation of H_2O in the reducing mantle transition zone.

284   Earth and Planetary Science Letters, 557, 116755.

285   Fei, H. (2021). Water content of the dehydration melting layer in the topmost lower mantle.

286   Geophysical Research Letters, 48, e2020GL090973.

287   Fei, H., and Katsura, T. (2020a). High water solubility of ringwoodite at mantle transition zone

288   temperature. Earth and Planetary Science Letters, 531, 115987.

289   Fei, H., and Katsura, T. (2020b). Pressure dependence of proton incorporation and water

290   solubility in olivine. Journal of Geophysical Research: Solid Earth, 125, e2019JB018813.

291   Fei, H., and Katsura, T. (2021). Water solubility in Fe-bearing wadsleyite at mantle transition

292   zone temperatures. Geophysical Research Letters, 48, e2021GL092836.

293   Fei, H., Yamazaki, D., Sakurai, M., Miyajima, N., Ohfuji, H., Katsura, T., and Yamamoto, T.

294   (2017). A nearly water-saturated mantle transition zone inferred from mineral viscosity.

295   Science Advances, 3, e1603024.

296 Fei, H., Koizumi, S., Sakamoto, N., Hashiguchi, M., Yurimoto, H., Marquardt, K., Miyajima, N.,

297   and Katsura, T. (2018). Pressure, temperature, water content, and oxygen fugacity

298   dependence of Mg grain-boundary diffusion coefficient in forsterite. American

299   Mineralogist, 103, 1354–1361.

300 Férot, A., and Bolfan-Casanova, N. (2012). Water storage capacity in olivine and pyroxene to 14

301   GPa: implications for the water content of the Earth's upper mantle and nature of seismic

302   discontinuities. Earth and Planetary Science Letters, 349-350, 218–230.

303 Frost, D.J. (2008). The upper mantle and transition zone. Elements, 4 (3), 171-176.

304 Fu, S., Yang, J., Karato, S., Vasiliev, A., Presniakov, M.Y., Gavrilliuk, A.G., Ivanova, A.G.,

305   Hauri, E.H., Okuchi, T., Purevjav, N., and Lin, J.F. (2019). Water concentration in single-

306   crystal (Al,Fe)-bearing bridgmanite grown from the hydrous melt: implications for

307   dehydration melting at the topmost lower mantle. Geophysical Research Letters, 46, 10346–

308   10357.

309 Geiger, C.A., and Rossman, G.R. (2018). IR spectroscopy and OH^- in silicate garnet: the long

310   quest to document the hydrogarnet substitution. American Mineralogist, 103(3), 384–393.

311 Guo, X., Bai, J., Wang, C., Wu, X., and Zhou, X. (2020). CO_2 induced a small water solubility in

312   orthopyroxene and its implications for water storage in the upper mantle. Journal of

313   Geophysical Research: Solid Earth, 125, e2019JB018745.

314 Hirschmann, M.M. (2006). Water, melting, and the deep Earth H_2O cycle. Annual Review of

315   Earth and Planetary Sciences, 1(34), 629–653.

316 Hirschmann, M.M., Aubaud, C., and Withers, A. C. (2005) Storage capacity of H_2O in nominally

317   anhydrous minerals in the upper mantle. Earth and Planetary Science Letters, 236, 167-181.

318   Irifune, T., and Ringwood, A.E. (1987). Phase transformations in primitive MORB and pyrolite

319   compositions to 25 GPa and some geophysical implication. In: Manghnani, M.H., Syono,

320   Y. (Eds.), High Pressure Research in Mineral Physics (pp.31-242). American Geophysical

321   Union, Washington, DC.

322   Ishii, T., Kojitani, H., and Akaogi, M. (2018). Phase relations and mineral chemistry in pyrolitic

323   mantle at 1600–2200 °C under pressures up to the uppermost lower mantle: phase

324   transitions around the 660-km discontinuity and dynamics of upwelling hot plumes. Physics

325   of the Earth and Planetary Interiors, 274, 127–137.

326   Ishii, T., Kojitani, H., and Akaogi, M. (2019). Phase relations of Harzburgite and MORB up to

327   the uppermost lower mantle conditions: precise comparison with Pyrolite by multisample

328   cell high-pressure experiments with implication to dynamics of subducted slabs. Journal of

329   Geophysical Research: Solid Earth, 124(4), 3491–3507.

330   Katayama, I., Hirose, K., Yurimoto, H., and Nakashima, S. (2003). Water solubility in majoritic

331   garnet in subducting oceanic crust. Geophysical Research Letters, 30(22), 2155.

332   Katsura, T., A revised adiabatic temperature profile in the mantle. (2022). Journal of

333   Geophysical Research: Solid Earth, 127, e2021JB023562.

334   Keppler, H., and Bolfan-Casanova. (2006). Thermodynamics of water solubility and partitioning.

335   Reviews in Mineralogy and Geochemistry, 62, 193-230.

336   Kohlstedt, D.L., Keppler, H., and Rubie, D.C. (1996). Solubility of water in the α, β, and γ

337   phases of $(Mg, Fe)_2SiO_4$. Contributions to Mineralogy and Petrology, 123, 345–357.

338   Litasov, K. (2010). The influence of Al_2O_3 on the H_2O content in periclase and ferropericlase at

339   25 GPa. Russian Geology and Geophysics, 51 (6), 644–649. doi:10.1016/j.rgg.2010.05.005

340   Litasov, K. D., Shatskiy, A., and Ohtani, E. (2013). Earth's mantle melting in the presence of C-

341   O-H bearing fluid. In: Karato, S. I. (Ed.), Physics and chemistry of the deep Earth (pp. 38–

342   65). John Wiley and Sons.

343   Litasov, K.D., Shatskiy, A., Ohtani, E., and Katsura, T. (2011). Systematic study of hydrogen

344   incorporation into Fe-free wadsleyite. Physics and Chemistry of Minerals, 38, 75–84.

345   Liu, Z., Fei, H., Chen, L., McCammon, C., Wang, L., Liu, R., Wang, F., Liu, B., and Katsura, T.

346   (2021). Bridgmanite is nearly dry at the top of the lower mantle. Earth and Planetary

347   Science Letters, 570, 117088.

348   Panero, W.R., Thomas, C., Myhill, R., Pigott, J.S., Raepsaet, C., and Bureau, H. (2020).

349   Dehydration melting below the undersaturated transition zone. Geochemistry, Geophysics,

350   Geosystems, 21(2).

351   Paterson, M.S. (1982). The determination of hydroxyl by infrared absorption in quartz, silicate

352   glass and similar materials. Bulletin de Minéralogie, 105, 20–29.

353   Pearson, D.G., Brenker, F.E., Nestola, F., McNeil, J., Nasdala, L., Hutchison, M.T., Matveev, S.,

354   Mather, M., Silversmit, G., Schmitz, S., Vekemans, B., and Vincze, L. (2014). Hydrous

355   mantle transition zone indicated by ringwoodite included within diamond. Nature, 507,

356   221–224.

357   Pigott, J.S., Wright, K., Gale, J.D., and Panero, W.R. (2015). Calculation of the energetics of

358   water incorporation in majorite garnet. American Mineralogist, 100(5-6), 1065–1075.

359   Purevjav, N., Okuchi, T., Tomioka, N., Abe, J., and Harjo, S. (2014) Hydrogen site analysis of

360   hydrous ringwoodite in mantle transition zone by pulsed neutron diffraction. Geophysical

361   Research Letters, 41, 6718–6724.

362   Purevjav, N., Okuchi, T., Tomioka, N., Wang, X., and Hoffmann, C. (2016) Quantitative

363   analysis of hydrogen sites and occupancy in deep mantle hydrous wadsleyite using single

364   crystal neutron diffraction. Scientific Reports, 6.

365   Purevjav, N., Tomioka. N., Yamashita, S., Shinoda, K., Kobayashi, S., Shimizu, K., Ito, M., Fu,

366   S., Gu, J., Hoffmann, C., Lin, J.F., and Okuchi, T. (2023) Hydrogen incorporation

367   mechanism   in   the   lower-mantle   bridgmanite.   American   Mineralogist,   doi:

368   https://doi.org/10.2138/am-2022-8680 (in press).

369   Revenaugh, J., and Sipkin., S.A. (1994) Seismic evidence for silicate melt atop the 410-km

370   mantle discontinuity. Nature, 369, 474–476

371   Ringwood, A.E. (1991). Phase transformations and their bearing on the constitution and

372   dynamics of the mantle. Geochimica et Cosmochimica Acta, 55, 2083–2110.

373   Schmandt, B., Jacobsen, S. D., Becker, T. W., Liu, Z., and Dueker, K. G. (2014). Dehydration

374   melting at the top of the lower mantle. Science, 344, 1265–1268.

375   Smyth, J.R., Frost, D.J., Nestola, F., Holl, C.M., and Bromiley, G. (2006). Olivine hydration in

376   the deep upper mantle: effects of temperature and silica activity. Geophysical Research

377   Letters, 33(15), 311–324.

378   Stixrude, L., and Lithgow-Bertelloni, C. (2007). Influence of phase transformations on lateral

379   heterogeneity and dynamics in Earth's mantle. Earth and Planetary Science Letters, 263, 45–

380   55.

381   Tan, E., Gurnis, M., and Han, L. (2002). Slabs in the lower mantle and their modulation of plume

382   formation. Geochemistry Geophysics Geosystems, 3, 1067.

383   Thomas, S., Wilson, K., Koch-Müller, M., Hauri, E.H., McCammon, C., Jacobsen, S.D., Lazarz,

384   J., Rhede, D., Ren, M., Blair, N., and Lenz, S. (2015). Quantification of water in majoritic

385   garnet. American Mineralogist, 100(5-6), 1084–1092.

386   Withers, A. C., and Hirschmann, M. M. (2008). Influence of temperature, composition, silica

387   activity, and oxygen fugacity on the H_2O storage capacity of olivine at 8 GPa. Contributions

388   to Mineralogy and Petrology, 156, 595–605.

389   Withers, A.C., Wood, B.J., and Carroll, M.R. (1998). The OH content of pyrope at high pressure.

390   Chemical Geology, 147(1), 161–171.

391   Vinnik, L., and Farra, V. (2007). Low S velocity atop the 410-km discontinuity and mantle

392   plumes. Earth and Planetary Science Letters, 2007, 262(3-4), 398–412.

393   Zhu, F., Li, J., Liu, J., Dong, J., and Liu, Z. (2019). Metallic iron limits silicate hydration in

394   Earth's transition zone. Proceedings of the National Academy of Sciences of the United

395   States of America, 116(45), 22526–22530.

396

397   **Table 1.** Nominal compositions of starting materials A, B, C, and D.

398

	A	B	C	D
SiO_2 (wt.%)	51.89	54.58	42.96	48.08
Al_2O_3 (wt.%)	12.17	7.01	5.52	6.17
FeO (wt.%)	2.94	2.97	3.98	3.54
MgO (wt.%)	23.67	19.07	25.57	22.71
CaO (wt.%)	9.33	16.37	21.95	19.49
H_2O (wt.%)	11.94	12.11	12.09	12.17

399

400

401   **Table 2.** A list of run conditions, phases in the recovered capsules, and water contents in

402   majorite based on various infrared calibrations. Mj: majorite, St: stishovite, Dm: davemaoite

403   ($CaSiO_3$ perovskite), hy-PhB: superhydrous phase B, PhD: phase D, Mgs: magnesite.

Run No.	Starting material	T (K)	Duration (h)	Phases present	τ (μm)	$^aC_{H_2O}$ (wt. ppm)	$^bC_{H_2O}$ (wt. ppm)	$^cC_{H_2O}$ (wt. ppm)
H5450	B	1670	24	Mj, St, Dm, melt	82	2591 (277)	2318 (248)	910 (92)
H5450	C	1670	24	Mj, hy-PhB, Mgs, PhD, melt	82	2913 (453)	2606 (405)	999 (122)
H5405	B	1870	24	Mj, St, melt	75	1423 (30)	1272 (27)	492 (16)
H5423	C	1870	20	Mj, Dm, melt	70	930 (157)	832 (140)	322 (64)
H5423	D	1870	20	Mj, Dm, melt	70	812 (168)	727 (151)	275 (57)
H5416	A	2070	20	Mj, St, melt	104	871 (64)	779 (57)	314 (17)
H5416	B	2070	20	Mj, St, melt	104	894 (90)	800 (81)	322 (32)
H5419	A	2270	4	Mj, St, melt	69	412 (74)	368 (66)	149 (27)
H5419	B	2270	4	Mj, melt	70	636 (289)	569 (259)	248 (136)

404   C_{H_2O}: the H_2O content in majorite

405   *a*: Based on Thomas et al. (2015) calibration.

406   *b*: Based on Bell et al. (1995) calibration.

407   *c*: Based on Paterson (1982) calibration.

408

409   **Table 3.** Chemical composition of the recovered majorite analyzed by EPMA.

410

| Run No.	N	Al_2O_3 (wt.%)	SiO_2 (wt.%)	MgO (wt.%)	CaO (wt.%)	FeO (wt.%)	Total (wt.%)	Al (atomic)	Si (atomic)	Mg (atomic)	Ca (atomic)	Fe (atomic)
H5450B	19	16.25 (0.3)	46.26 (0.2)	26.10 (0.29)	7.68 (0.32)	2.86 (0.11)	99.15 (0.38)	1.35 (0.02)	3.25 (0.01)	2.73 (0.02)	0.58 (0.03)	0.17 (0.01)
H5450C	21	15.88 (0.36)	46.10 (0.20)	25.41 (0.32)	8.40 (0.38)	3.71 (0.26)	99.49 (0.33)	1.32 (0.03)	3.25 (0.01)	2.67 (0.03)	0.63 (0.03)	0.22 (0.02)
H5405B	12	15.81 (0.29)	46.53 (0.26)	21.50 (0.45)	12.96 (0.27)	2.20 (0.05)	99.01 (0.41)	1.32 (0.02)	3.31 (0.02)	2.28 (0.04)	0.99 (0.02)	0.13 (0.00)
H5423C	19	9.75 (0.48)	50.12 (0.31)	26.25 (0.27)	10.47 (0.21)	3.06 (0.10)	99.65 (0.33)	0.81 (0.04)	3.53 (0.02)	2.75 (0.03)	0.79 (0.02)	0.18 (0.01)
H5423D	16	10.86 (0.50)	48.26 (0.40)	24.39 (0.41)	11.97 (0.35)	3 .90 (0.14)	99.37 (0.24)	0.92 (0.04)	3.44 (0.02)	2.59 (0.04)	0.91 (0.03)	0.23 (0.01)
H5416A	10	17.54 (0.35)	46.38 (0.36)	26.96 (0.27)	6.34 (0.2)	2.48 (0.12)	99.70 (0.39)	1.44 (0.03)	3.22 (0.02)	2.79 (0.02)	0.47 (0.02)	0.14 (0.01)
H5416B	13	15.47 (0.90)	46.50 (0.37)	22.15 (0.38)	12.49 (0.53)	2.48 (0.18)	99.09 (0.39)	1.30 (0.07)	3.31 (0.03)	2.35 (0.04)	0.95 (0.04)	0.15 (0.01)
H5419A	16	20.51 (0.41)	44.72 (0.18)	26.78 (0.15)	4.77 (0.20)	1.94 (0.10)	98.70 (0.33)	1.68 (0.03)	3.11 (0.01)	2.78 (0.02)	0.36 (0.02)	0.11 (0.01)
H5419B	15	11.06 (0.72)	49.21 (0.36)	26.39 (0.40)	10.47 (0.57)	1.92 (0.10)	99.06 (0.25)	0.92 (0.06)	3.47 (0.03)	2.77 (0.03)	0.79 (0.05)	0.11 (0.01)

411   The data in parentheses are one standard deviation of the N analyzed points for each sample. The FeO content in

412   wt.% is obtained by assuming all iron to be ferrous.

413

414 **Table 4.** Chemical composition of the melt analyzed by EPMA.

415

Run No.	N	Al_2O_3 (wt. %)	SiO_2 (wt. %)	MgO (wt. %)	CaO (wt. %)	FeO (wt. %)	Total (wt. %)
H5450B	8	1.9(0.3)	17.9(2.8)	16.9(1.7)	4.5(0.6)	26.1(2.4)	67.2(1.4)
H5450C	14	1.9(0.5)	13.4(1.6)	20.0(2.7)	5.0(0.7)	24.5(2.3)	64.7(1.3)
H5405B	17	2.4(1.0)	31.7(2.2)	18.5(2.2)	3.9(0.3)	21.7(2.0)	78.1(2.5)
H5423C	10	0.8(0.1)	28.8(1.3)	20.4(1.9)	3.4(0.5)	26.3(1.9)	79.7(1.5)
H5423D	11	0.8(0.1)	20.4(1.3)	24.2(1.7)	3.6(0.2)	25.8(1.6)	74.8(1.3)
H5416A	10	1.9(0.2)	21.1(2.0)	17.6(2.4)	4.7(0.2)	23.9(1.7)	69.2(2.1)
H5416B	10	2.2(0.4)	30.2(1.5)	21.0(1.7)	3.8(0.2)	19.2(0.8)	76.4(1.2)
H5419A	8	4.2(0.3)	28.4(0.9)	13.7(0.5)	3.9(0.3)	20.2(0.5)	70.5(1.8)
H5419B	15	1.3(0.1)	35.0(1.1)	18.3(1.5)	2.7(0.1)	30.6(1.2)	87.8(0.7)

416 The data in parentheses are one standard deviation of the N analyzed points for each sample. The FeO content in

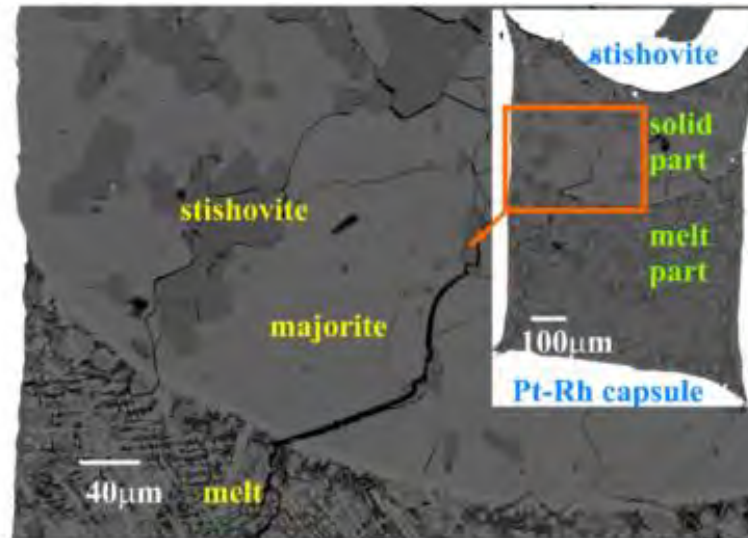417 wt.% is obtained by assuming all iron to be ferrous.

418

419

420   **Figure 1.** (a) Micro-focused XRD pattern taken on the recovered sample H5405B. (b) BSE

421   image of the sample H5405B. Majorite, stishovite, and quenched melt coexist in the sample

422   capsule. Mj: majorite. St: stishovite.
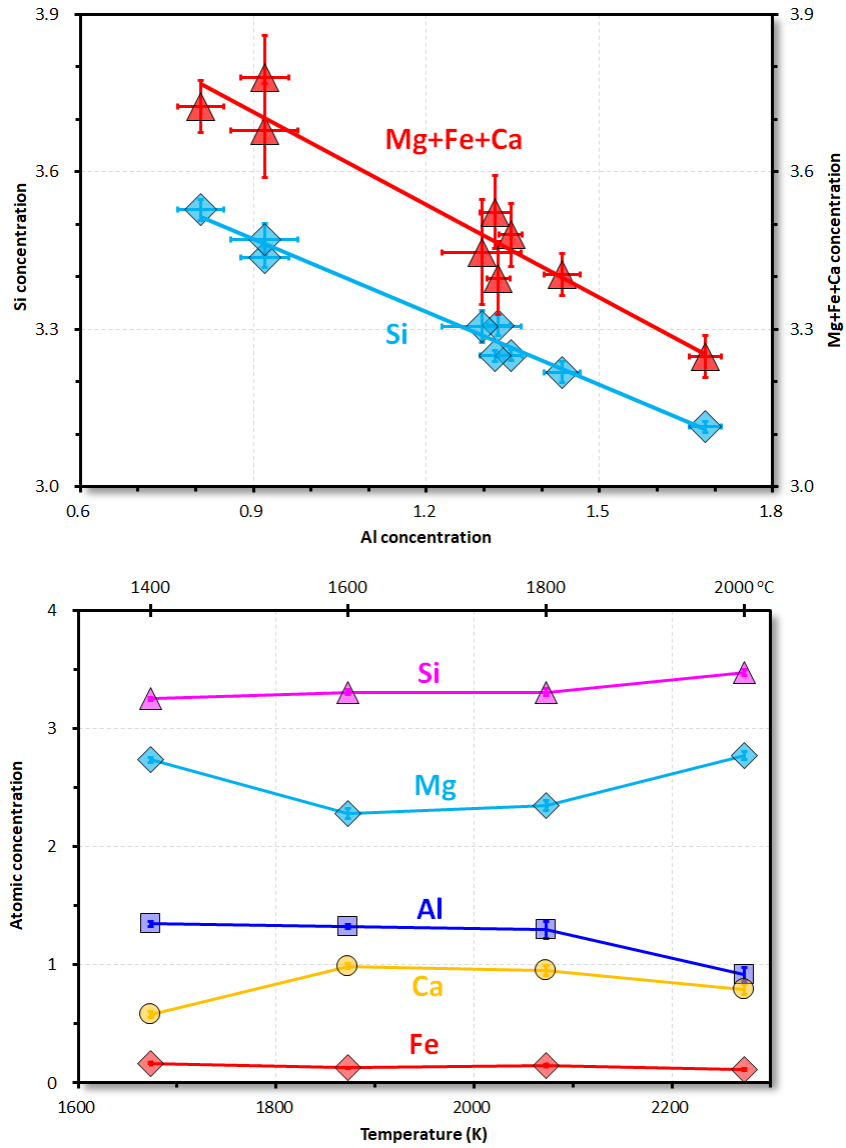
423
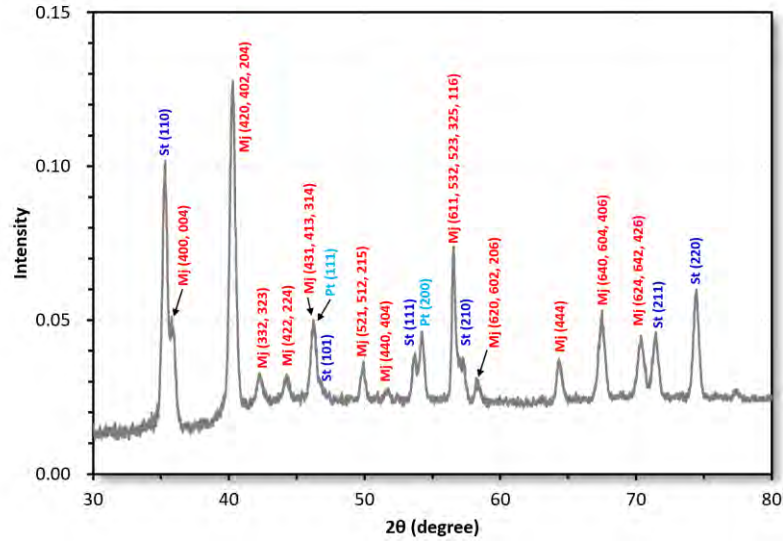
424

425

426

427   **Figure 2.** (a) The relationships of Si (blue symbols) and Mg+Fe+Ca (red symbols) to Al atomic

428   contents in majorite. (b) The temperature dependences of Si, Mg, Fe, Ca and Al contents in

429   majorite synthesized from the same starting material.

430

431
432

433

25

434   **Figure 3.** FTIR spectra of the samples after baseline subtraction and thickness normalization to 1

435   cm. The peaks at ~3615 cm^{-1} and ~3430 cm^{-1}, and fitting curves are obtained by leastsquares

436   fitting of the FTIR spectra, and represent the infrared absorption bands of majorite,

437   noncrystalline OH, and their summation, respectively.
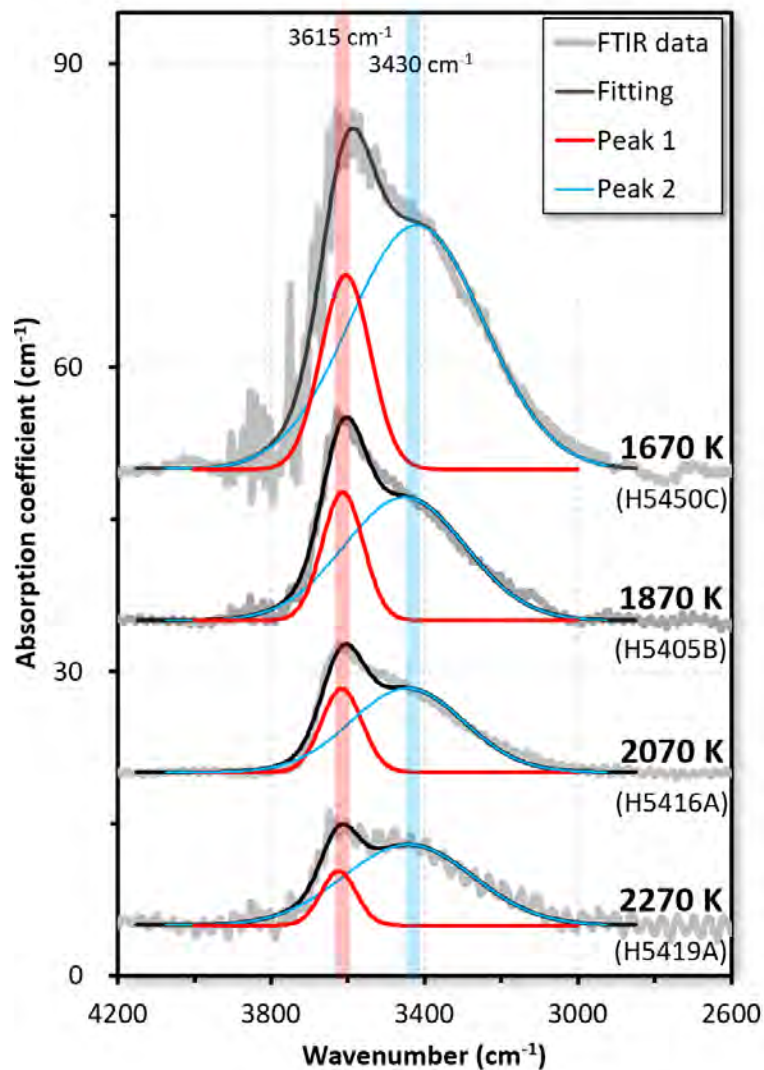
438

439 **Figure 4.** Temperature dependence of H_2O contents in majorite in the recovered samples and

440 comparison with previous studies. The data points from this study are based on the Thomas et al.
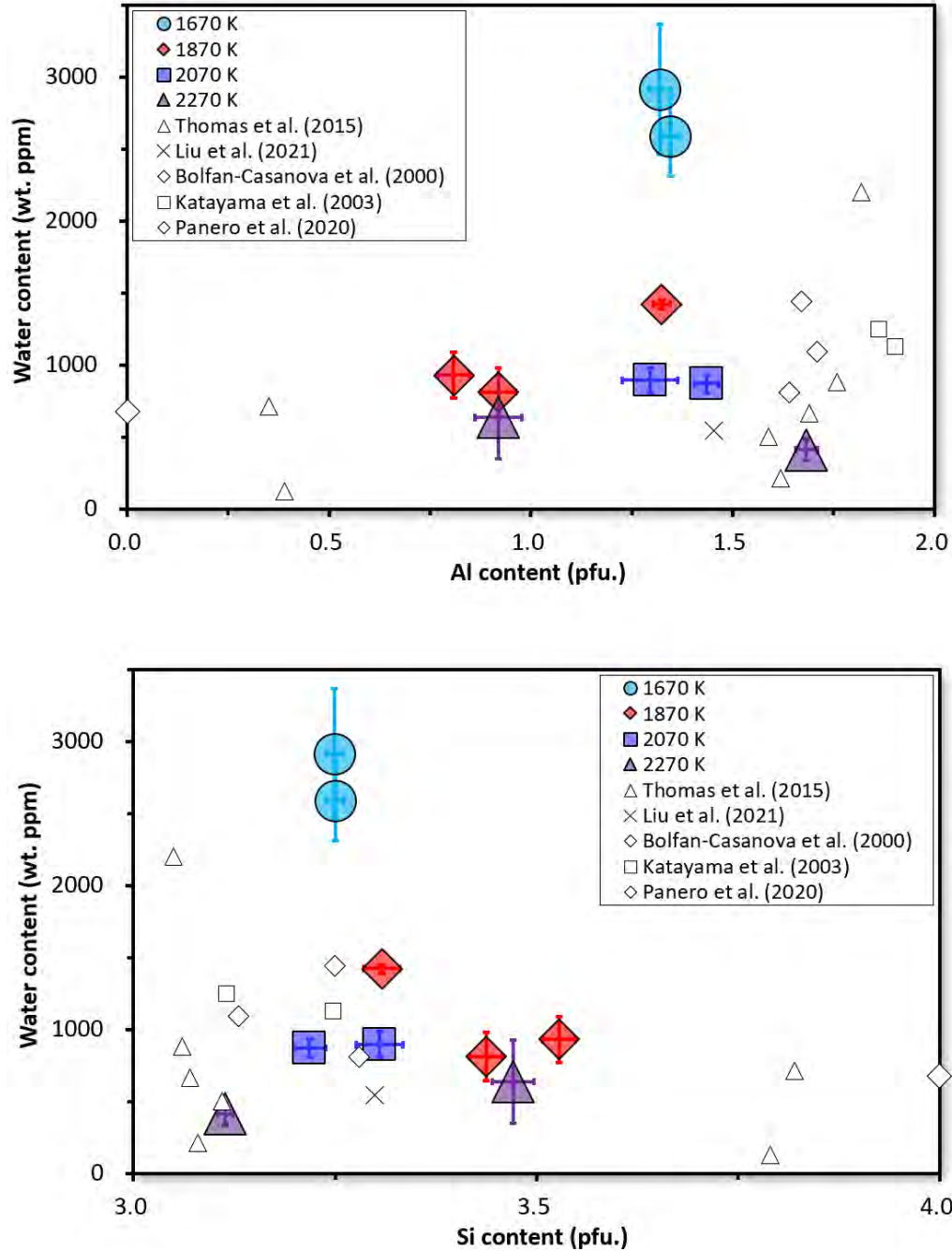
441 (2015) FTIR calibration.
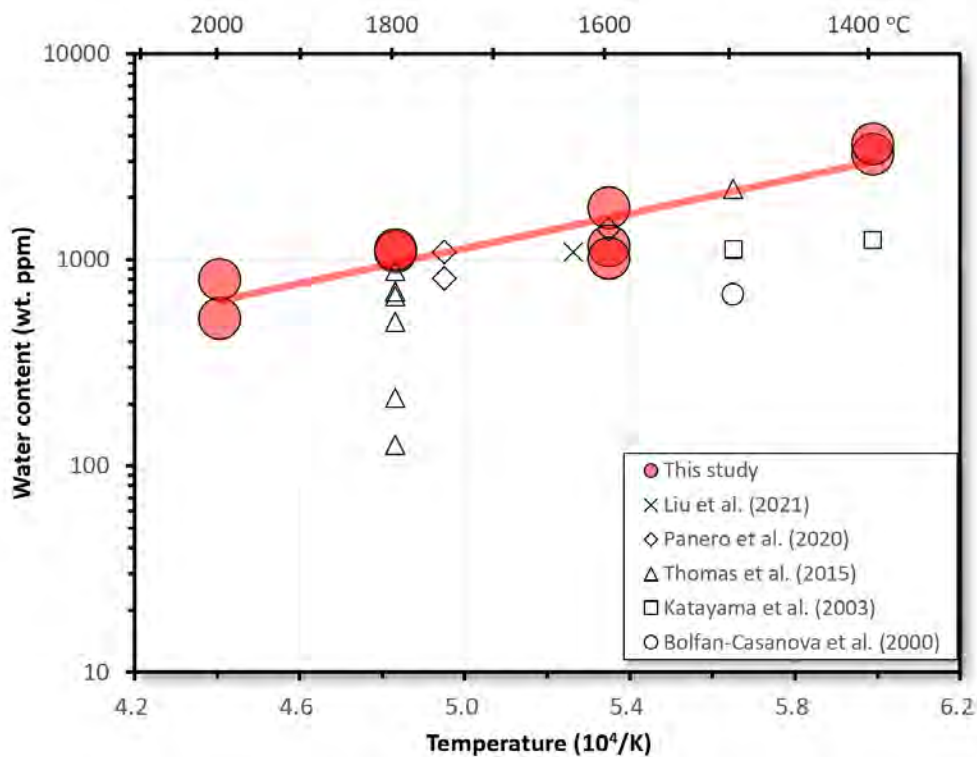
442

443

444　**Figure 5.** Compositional dependence of H_2O content in majorite. (A) Al content dependence. (B)

445　Si content dependence.

446

447